

# THE INFLUENCES OF EXTREMELY STRONG WIND

17A-06

## ON RADAR OBSERVATIONS

Pao-Liang Chang\*, Pin-Fang Lin, Wei-Ting Fang,  
and Yu-Shuang Tang

Central Weather Bureau, Taipei, Taiwan

### ABSTRACT

Extremely strong winds frequently damage radar systems, especially the radome and antenna. Even if the radar radome can resist extremely strong winds, radar tower vibrations could reduce the quality of radar observations. The intense wind speed influences on radar observations are investigated in this study based on the Ishigaki C-band Doppler radar operated by the Japan Meteorological Agency (JMA). During the passage of Typhoon Goni (2015) near Ishigaki Island, an extremely strong wind with a maximum gust wind speed of  $71 \text{ m s}^{-1}$  was observed. The radar recorded elevations that oscillated with a maximum amplitude of  $0.4^\circ$  at  $-0.1^\circ$  elevation, and the oscillation phenomenon was reflected in the reflectivity and Doppler velocity fields as Goni's eyewall encompassed Ishigaki Island.

The main oscillation period is approximately 0.25-0.33 seconds given an antenna rotational speed of  $\sim 4$  rpm (revolutions per minute) using a Fast Fourier Transform (FFT) analysis. There are two antenna oscillation periods that occurred on 23 Aug., one occurred from approximately 1030-1200 UTC, and the other occurred from 1330-1430 UTC. Between these two oscillation periods, the oscillation phenomenon stopped because Goni's eye moved over the radar site. Relative to the oscillation in the reflectivity field, the antenna oscillation exhibits a feature that is out of phase and generally consistent with the vertical reflectivity profile. The antenna oscillation influences on the Doppler velocity field are partially mitigated due to the presence of less vertical varieties. The influence of antenna oscillations on radar observations could be mitigated using the QC procedure by filtering the high wave numbers from wave numbers 45-60.

## 1. INTRODUCTION

Extremely strong winds frequently damage electric power supplies, communications, and radar hardware. In regard to damage to the radar radome and antenna, the WSR-88D Doppler radar operated by the Central Weather Bureau of Taiwan at Wu-Feng-San was destroyed by Typhoon Herb (1996), which had maximum sustained surface winds of  $65 \text{ m s}^{-1}$  (Wu et al. 2002). In 2013, super Typhoon Haiyan made landfall near Guiuan in the eastern-central Philippines and the radar pedestal in Guiuan was sheared off with 1-min sustained winds that were possibly as high as  $91 \text{ m s}^{-1}$  (Velden et al. 2017). In 2017, the WSR-88D radar operated by the National Weather Service (NWS) was destroyed by Hurricane Maria's powerful winds with an operational 1-min maximum sustained wind speed intensity estimate of  $70 \text{ m s}^{-1}$  as the hurricane moved onshore in southeastern Puerto Rico (Garcia-Rivera 2018).

Typhoon Goni (2015) was observed by the Ishigaki (ISHI) C-band Doppler radar operated by the Japan Meteorological Agency (JMA) at Ishigaki Island during its rapid intensification. As Goni passed near Ishigaki Island between approximately 1000 UTC and

1400 UTC, the radar eyewall area and eye moved over the radar site. The maximum estimated strong wind from the Doppler velocity exceeded  $70 \text{ m s}^{-1}$ , which resulted in an unusual oscillation pattern occurring in both the reflectivity and Doppler velocity fields. In this study, the characteristics of the reflectivity oscillations caused by antenna vibration and the wind speed criterion for oscillation occurrence are analyzed. The antenna vibration influences on the radar observations will also be investigated and discussed.

The data and methodology are described in the following section. The characteristics of the radar reflectivity and Doppler velocity fields in association with antenna vibrations will be analyzed in section 3. In section 4, the antenna oscillations and associated influences on the radar observations will be discussed. Finally, the conclusions are provided in section 5.

## 2. DATA AND METHODOLOGY

### 2.1 Data

The C-band Doppler radar ISHI operated by JMA at Ishigaki Island is used in this study. The radar data from Typhoon Goni between 0700 UTC and 1700 UTC 23 Aug 2015 are chosen to investigate the influences of extremely strong wind on radar observations. The radar ISHI is operated both in surveillance and Doppler mode with a total of 25 elevations obtained in 10 minutes. The scan

---

\* Corresponding author address: Pao-Liang Chang, Central Weather Bureau, Taipei, Taiwan; e-mail: [larkdi@cwb.gov.tw](mailto:larkdi@cwb.gov.tw).

strategies of ISHI include two surveillance modes for lower elevations and two Doppler modes for lower elevations and lower to upper elevations. These four scan modes are alternately operated and updated every 10 min. To more closely analyze the data from different elevations over time, the chosen data from the first surveillance mode were started approximately every 3 min within a 10 min period chosen for reflectivity analyses, and the data from Doppler mode are used for the wind analyses.

The ISHI radar is operated in dual-pulse repetition frequency (PRF) mode (Dazhang 1984; Frush 1991) to extend the maximum unambiguous velocity. Although the Nyquist velocity can reach  $52.71 \text{ m s}^{-1}$ , the Doppler velocity field would still encounter the folding problem under strong wind condition, especially in eyewall region. Therefore, the vortex-based Doppler velocity dealiasing algorithm (VDVD) is applied to recover the aliased Doppler velocities (Chang et al. 2019). In addition, data from nine weather stations gathered from the Ishigaki, Miyako, Iriomote, and Yonaguni Islands operated by JMA are selected to analyze the variations in surface winds. Three stations are within 150 km of the radar ISHI and are beneficial for investigating the evolution of wind speeds and directions during Typhoon Goni's passage.

## 2.2 FFT Analyses

Based on the recorded radar data from each beam, the wave numbers of antenna oscillations centered at the radar site with different ranges and elevations are analyzed using the Fast Fourier Transform (FFT) algorithm (Heideman et al. 1984). There are 512 beams for the radar ISHI Plan Position Indicator (PPI) scan with an azimuthal resolution of approximately  $0.7^\circ$ . A one-dimensional spatial FFT decomposes the oscillation signals into a series of wavenumbers associated with a given radius and elevations. Given the rotational speed of the radar antenna, the predominant oscillation periods (frequencies) can be determined by selecting the wave numbers of crucial components. The characteristic reflectivity oscillations caused by antenna vibrations and the wind speed criterion for the oscillation occurrence will be analyzed. The QC procedures based on oscillation conditions are also examined using a high-pass filter (Warde and Torres 2017).

## 2.3 VAD Analyses

The representative weather station Ishigaki is located near sea level and approximately 9.5 km southwest of the ISHI radar site. The ISHI radar is located near the top of Mt. Omoto-dake (525.5 m above sea level). Because there are no wind observations available at the radar site, a VAD (Lhermitte and Atlas 1962; Browning and Wexler 1968) was proposed to estimate wind information. Although the uniform flow assumption in the VAD algorithm cannot generally be satisfied with the flow characteristics of tropical cyclones, it can be conditionally applied if the VAD analysis areas are

limited to small ranges where they are close to the radar. Consequently, VAD analyses ranging from 1 km at  $1.1^\circ$  elevation are conducted to estimate the winds around the ISHI radar site during Typhoon Goni's passage.

## 3. RESULTS

### 3.1 Radar Observations

Figure 1 shows a reflectivity example at a  $-0.1^\circ$  elevation from the radar ISHI at 1150 UTC on 23 Aug 2015. The eyewall structure is well organized with a radius of 25 km and width of approximately 10-15 km, while the eastern part of the eyewall covers the radar site. The regular radial pattern with alternating strong and weak features is very pronounced, while this periodic pattern nearly encompasses the eyewall, moat and spiral rainband regions. The maximum difference in reflectivity can reach 30 dB in the azimuthal directions between 3 and 6 degrees. The other azimuths also present similar features, but the amplitudes are slightly smaller. At  $0.2^\circ$  elevation, the oscillation phenomenon is still obvious but mainly occurs along the moat region with amplitudes that generally decrease to 5-10 dB. The phenomenon can still be found, but at  $2.7$  and  $4.0$  degrees, the reflectivity intensities are generally weak in comparison with the reflectivity at lower elevations. The regular oscillation signals occur in limited areas around the outer rain band regions. Figure 2 and Fig. 3 show the evolution of the reflectivity and Doppler velocity fields every 30 min at  $0.2^\circ$  elevation during Typhoon Goni's passage near Ishigaki Island. The regular radial pattern in the reflectivity already exists in the moat region at 1120 UTC (Fig. 2a), but the amplitude of the oscillation phenomenon is relatively smaller than that at 1150 UTC (Fig. 2b). At 1220-1320 UTC (Fig. 2c and 2d), the oscillation phenomena disappear while the radar site enters the outer boundary of the eye region. At 1350 UTC (Fig. 2e), the oscillation phenomenon is present again, but the strength of the signal clearly decreases. At 1420 UTC (Fig. 2f), the oscillation phenomenon disappears as Typhoon Goni moves continuously northwestward and is far from the radar site. In addition, the eye and eyewall are characterized by polygonal shapes and rotated with time, suggesting that the phenomena may be related to the vortex Rossby wave, as mentioned in many studies, which indicates that the typhoon is potentially undergoing an intensification (e.g., Kuo et al. 1999; Kossin and Schubert 2001; Yang et al. 2007) that is consistent with the intensity analysis of Typhoon Goni, as shown in Shimada et al. (2018).

For the corresponding Doppler velocity field, it is noticeable that the eyewall region is characterized by an approximately symmetric dipole signature with a maximum magnitude of greater than  $60 \text{ m s}^{-1}$  at 1120 UTC at a  $0.2^\circ$  elevation (Fig. 3a). Outside the eyewall region, there are alternating positive and near zero value features in the moat and spiral rain band region,

which is located in the northern quadrant of the typhoon. A similar but slightly weaker oscillation signature can also be found in the spiral rainband region in the southern quadrant of the typhoon. The maximum magnitudes decrease dramatically with time from 1220 UTC to 1320 UTC (Figs. 3c to 3d) because of the Doppler velocity distortion, while the typhoon's eyewall covers the radar site due to the geometric limitation (Wood and Brown 1992). Consequently, the maximum typhoon wind speed estimated from the observations of the maximum/minimum Doppler velocities would be underestimated depending on the degrees of geometric distortion. After 1350 UTC (Fig. 3f), the maximum/minimum inbound/outbound Doppler velocities are comparable to those at 1120 UTC to 1150 UTC because the eyewall region gradually moves away from the radar site and the geometric limitation disappears. Similar to the reflectivity field shown in Fig. 1, the oscillation phenomenon of the Doppler velocity is not obvious due to the smaller vertical varieties covering the radar during the eyewall. Consistent with the reflectivity field shown in Fig. 3, the most pronounced oscillation phenomena in the Doppler velocity field at an elevation of  $0.2^\circ$  occur before 1150 UTC and after 1420 UTC. Because the radar is situated on a mountain top on Ishigaki Island, which is less than 10 km from the coastline, serious sea clutters frequently occur in the radar observations, especially under strong wind conditions that frequently result from severe weather events, such as tropical cyclones (e.g., Ryzhkov et al. 2002; Chang et al. 2009). Consequently, the pronounced oscillation phenomena in the Doppler velocity are caused by the large differences between Typhoon Goni's circulation and the sea clutter signals. The oscillation phenomena disappear while the radar site enters the outer boundary of the eye region between 1220 UTC and 1320 UTC.

### 3.2 Oscillation Analyses

The significant antenna oscillation substantially affects the radar observation, as shown in Fig. 2 and Fig. 3. To analyze the oscillation characteristics in the reflectivity field, a FFT analysis is used to decompose the oscillation signals into a series of wavenumbers from 0 to 200 associated with a given radius and elevations. Figure 4 shows an example of the azimuthal distribution of reflectivity with a 50 km radar site range at 1150 UTC at a  $-0.1^\circ$  elevation. The reflectivity intensities range from 4 to 47 dBZ for all azimuths. The high frequency oscillation also occurs in the azimuthal distribution with a maximum amplitude of 15 dB at approximately  $0^\circ$  azimuth (to the north). The curve composed of the FFT analysis wave numbers can fit the reflectivity data well. With the FFT analysis of the elevation azimuthal distribution (Fig. 5), the maximum amplitude reached  $0.4^\circ$ . Similar to the results in the FFT analysis of the reflectivity oscillation (Fig. 4), the curve composed of the wave numbers FFT analysis can also fit well with the elevation data recorded from each beam.

Consequently, the FFT analysis can be adequately applied to decompose the reflectivity perturbation signal into a series of wave numbers.

From the analyses of elevation amplitudes with different wave numbers and preset elevations from  $-0.44^\circ$  to  $4.0^\circ$  (7 elevations) (Fig. 6), the amplitudes greater than  $0.03^\circ$  almost always occur at wave numbers 45 to 60 for all elevations. Based on the given radar ISHI antenna rotational speed of 4 rpm, the corresponding frequencies (periods) are from  $3 \text{ s}^{-1}$  (0.33 s) to  $4 \text{ s}^{-1}$  (0.25 s). In addition, the maximum elevation amplitude is found at the  $-0.1^\circ$  elevation at a value greater than  $0.08^\circ$ . The antenna oscillation influenced all elevations, especially the lower elevations. Reflectivity amplitudes with different wave numbers (filter out wave numbers  $< 20$ ) and elevations from  $-0.44^\circ$  to  $4.0^\circ$  are shown in Fig. 7. The larger reflectivity amplitudes are confined at elevations  $< 0.2^\circ$ , and the maximum reflectivity amplitude larger than 4 dB occurred at  $-0.1^\circ$ , with wave numbers between 45 and 50. The reflectivity amplitude characteristic is consistent with the reflectivity analyses, as shown in Fig. 4. The higher elevation oscillation signals that are predominantly caused by the vertical reflectivity varieties are relatively nonsignificant, as documented in section 3a.

For further analysis, wave numbers from 45 to 60 are composed to investigate the phase relationship between the antenna oscillation and reflectivity oscillation. Despite the amplitude and unit differences between the elevation and reflectivity, the out of phase signature (Fig. 8) and negative correlation with a correlation coefficient of  $-0.68$  (not shown) are found between the distributions of antenna oscillation and reflectivity oscillation. The feature indicates that the reflectivity values would decrease (increase) while the antenna elevations increase (decrease) during the period of antenna oscillation. Maximum antenna amplitudes from wave numbers ranging from 45-60 are also chosen to illustrate the temporal evolution of antenna oscillations (Fig. 9). There are two periods occurring between 1010 UTC and 1210 UTC and between 1340 UTC and 1430 UTC for maximum antenna amplitudes greater than approximately  $0.02^\circ$  (blue line in Fig. 9). These two periods generally agree with the occurrences of oscillation phenomena in the reflectivity field, as mentioned in section 3a. In addition, the antenna amplitudes for wave numbers 1 and 2 are generally larger during the two aforementioned periods with amplitudes of approximately  $0.01$ - $0.02$  degrees, illustrating that the oscillations are not only concentrated at high frequency regions but also at low frequency regions during the antenna oscillations, which are possibly related to the radar tower vibration and mechanical inertia of the radar antenna, as can be verified with further investigations of wind tunnel experiments.

### 3.3 Surface Observations

Several islands, including Miyako, Iriomote, and Yonaguni Islands within 150 km of Ishigaki Island, provide surface observations during Typhoon Goni's passage. In total, the available data from nine surface stations are selected to investigate the spatial-

temporal variations in surface winds (Fig. 10a). Figure 10b shows the temporal distributions of 10-min sustained and gust wind speeds and pressure observed at Ishigaki station (94081) on southwestern Ishigaki Island between 0000 UTC Aug 23 and 0000 UTC Aug 24. Sustained and gust wind speeds gradually increase while the pressure gradually decreases. The maximum sustained and gust wind speeds are above  $45 \text{ m s}^{-1}$  and  $70 \text{ m s}^{-1}$  at 1200 UTC and 1400 UTC, respectively, while the minimum pressure of approximately 945 hPa occurs at approximately 1300 UTC. On southeastern Ishigaki Island, the sustained and gust wind speeds at station 94086 show similar distributions to those at station Ishigaki. The maximum sustained and gust wind speeds are approximately  $50 \text{ m s}^{-1}$  and  $70 \text{ m s}^{-1}$ , respectively (Fig. 10c). The maximum gust wind speed occurs at approximately 1400 UTC. At station 94001, located in the northeastern part of Ishigaki Island, there are two double peaks found during Typhoon Goni's passage (Fig. 10d). The maximum sustained and gust wind speeds are approximately  $40\text{-}45 \text{ m s}^{-1}$  and  $55\text{-}60 \text{ m s}^{-1}$  at approximately 1230 UTC and 1500 UTC, respectively. The wind speeds are slightly weaker than the two abovementioned stations, which are possibly caused by the station being relatively far away from the typhoon's center, and the station location is on the lee side of Mt. Omoto-dake.

### 3.4 VAD Winds

As mentioned above, the representative surface station Ishigaki is located near sea level and approximately 9.5 km southwest of the radar site. Therefore, a VAD analysis is conducted with Doppler velocity data to estimate the wind speed around the radar site. Figure 11 shows examples of the VAD analysis for 1 km radial range at  $1.1^\circ$  elevation from 1100 UTC to 1400 UTC. The maximum inbound (outbound) Doppler velocity is approximately  $68 \text{ m s}^{-1}$  ( $70 \text{ m s}^{-1}$ ) for all analyzed radial ranges at 1100 UTC, and the radar site is covered by Typhoon Goni's eyewall (Fig. 11a). As the radar site entered Typhoon Goni's eye region at 1200 UTC, the maximum outbound velocities dramatically decreased to approximately  $50 \text{ m s}^{-1}$ , and the maximum inbound velocities are more scattered, with values of  $45\text{-}60 \text{ m s}^{-1}$  (Fig. 11b). The maximum outbound and inbound velocities dropped significantly with a wind speed of  $\sim$ approximately  $20 \text{ m s}^{-1}$  at 1300 UTC (Fig. 11c). The maximum inbound (outbound) velocities increase with values of approximately  $70 \text{ m s}^{-1}$  at 1400 UTC when the radar site is again covered by the eyewall during Typhoon Goni's northeastward movement (Fig. 11d). Compared with the observations from the weather stations on Ishigaki Island (Fig. 10a), the wind speeds retrieved from the VAD analysis are close to the surface gust wind speeds before 1200 UTC and after 1500 UTC (Fig. 10b). Between 1200 UTC and 1500 UTC, there is a dramatic difference with a maximum value of  $50 \text{ m s}^{-1}$  between the VAD and surface winds, even though the station is only approximately 9.5 km southwest of the radar site. It is speculated that the radar site already entered the eye region, but the

surface station is still affected by Typhoon Goni's eyewall so that the high wind speeds remain. The other two stations, 94086 and 94011, on Ishigaki Island (Figs. 10c and 10d) show large differences between the VAD and surface wind speeds. The times of peak wind speed occurrence from the VAD analysis presents an approximately 1-2 hour lag relative to those from the surface wind speeds observed at station 94086 as the eyewall approached. Because station 94086 is situated in the plain area south of the island (Fig. 10c), the wind speed distributions are similar to those at station 94081, with a maximum wind speed of  $\sim 66 \text{ m s}^{-1}$ . However, there are approximately  $5\text{-}20 \text{ m s}^{-1}$  differences as the eyewall affects the radar site, but the station is still outside the eyewall region. Therefore, there is a near two-hour lag in the peak wind speed occurrence. For station 94011, located on northeastern Ishigaki Island, there are double peaks of wind speeds, indicating that the station is significantly affected twice by the eyewall (Fig. 10c). However, the wind speeds are relatively low, with values of  $50\text{-}55 \text{ m s}^{-1}$ , which possibly result from the station being situated on the lee side of the mountain Omoto-dake and the wind speeds could be slowed down by the blocking effect. After the eyewall gradually moves away from Ishigaki Island, the differences between the wind speeds from the surface observations and VAD analysis significantly decrease. Generally, the location and altitude differences potentially result in wind speed differences between the radar site and weather stations. The structure (shape, intensity, and so on) and movement of the typhoons also contributes to the wind speed differences.

Figure 12 shows examples of the spatial wind distributions from the surface observations and VAD analysis from 1050 UTC to 1450 UTC, which overlap with the reflectivity at a  $-0.1^\circ$  elevation. The surface and VAD winds show the obvious cyclonic circulation. The maximum wind speeds from the surface observations are approximately  $60\text{-}65 \text{ m s}^{-1}$  in the eyewall region and as low as  $20 \text{ m s}^{-1}$  outside of the rainband region at 1050 UTC and 1150 UTC, respectively (Fig. 12a and Fig. 12b). The wind speeds and directions retrieved from the VAD analysis are generally comparable to the surface observations. The wind distributions outside the eyewall region are not significantly changed, but the VAD wind significantly decreases to approximately  $20 \text{ m s}^{-1}$ , and the surface winds are still strong, with speeds of  $45\text{-}63 \text{ m s}^{-1}$  on Ishigaki Island at 1250 UTC (Fig. 12c). The VAD wind increases to approximately  $53 \text{ m s}^{-1}$  when the southern part of the eyewall affects the radar site at 1350 UTC (Fig. 12d). Subsequently, the surface and VAD winds decrease to  $35\text{-}40 \text{ m s}^{-1}$  (not shown) when the eyewall moves northeastward and gradually further away from the surface stations and the radar site on Ishigaki Island, while the wind speeds increase from the surface stations located on the northeastern islands of Ishigaki Island.

## 4. DISCUSSION

### 4.1 Antenna Oscillations

Based on the building vibrations, the height of the building is generally proportional to the oscillation period for a building lower than 50 m (Lagos and Kupeer 2012; Xu et al. 2014). The empirical formula of the fundamental vibration period  $T$  (s) can be expressed by the following equation:

$$T=0.014 H \sim 0.025 H \quad (1)$$

where  $H$  (m) is the height of the building. The tower height of the radar ISHI is 17.5 m above ground level (AGL). According to the empirical formula, the fundamental vibration periods are equal to 0.245-0.435 s. The predominant period analyzed from the reflectivity observations is 0.33 s. Therefore, the results essentially agree with the expectation of wind-induced vibrations on buildings, illustrating that the taller the tower is, the longer the wind-induced vibration or oscillation will be.

With the maximum amplitudes of elevations from wave numbers 45-60 greater than approximately  $0.02^\circ$  occurring between 1010 UTC and 1210 UTC and between 1340 UTC and 1430 UTC during Typhoon Goni, it is suggested that the minimum wind speed criterion for the occurrence of the antenna oscillation is approximately  $50 \text{ m s}^{-1}$ . In addition, the wind speeds from the VAD analysis are close to the surface gust winds and are consistent with the occurrence times of the reflectivity oscillations. Consequently, it is suggested that the wind speed criterion for the antenna oscillation occurrences is approximately  $50 \text{ m s}^{-1}$  for the ISHI radar. However, the wind speed criteria for the wind-induced antenna oscillation result from the vibrational effect of the buildings that are closely related to the structure, material, height, and weight of the radar tower (Xu et al. 2014). The vibrational effect could be adequately mitigated if extremely strong wind conditions are considered during the design of radar towers.

### 4.2 Influences on Radar Observations

As shown in section 3a, the radar tower oscillates with a maximum wind speed of greater than  $50 \text{ m s}^{-1}$ , which results in the antenna oscillation occurrence and subsequently influences the data quality of the radar observations. From the reflectivity differences between consecutive elevations, the reflectivities at the  $-0.1^\circ$  elevation are generally 1.5 dB higher than those at the  $0.2^\circ$  elevation. The differences are mainly attributed to the middle intensities at approximately 20-30 dBZ (not shown). There is no remarkable difference when the reflectivity is greater than 40 dBZ between the  $-0.1$  and  $0.2^\circ$  elevation observations due to less vertical variety, as shown in Fig. 2. The differences in the upper elevations between 2.7 and 4.0 degrees show no significant bias. It is implied that the oscillation phenomenon in the reflectivity would be substantially mitigated due to less vertical variations at these two elevations.

As analyzed above, the perturbation signals can be decomposed into a series of wavenumbers associated with the given radii and elevations using a

FFT analysis. To mitigate the influences of antenna oscillations on the radar observations, a QC procedure is proposed using a high-pass filter. Because the vertical profiles of reflectivity are strongly related to precipitation types (ex: convective and stratiform) and nonweather echoes such as ground and sea clutter, especially for sea clutter from coastal radars, the QC procedure would potentially be biased due to the vertical varieties. Therefore, data from the elevation differences smaller than  $0.1^\circ$  are used to calculate the mean reflectivity and then replace the wave number 0 in the FFT analysis to mitigate the mean reflectivity biases. Figure 13a shows examples of reflectivity at the  $-0.1^\circ$  elevation at 1150 UTC after the proposed QC procedure by filtering out wave numbers 45 to 60. Although there are still weak signals found in the moat and spiral rainband regions, the features of regular radial patterns are apparently mitigated. Higher elevation at the  $0.2^\circ$ , a better performance is shown for mitigating the oscillation features after the QC procedure due to the vertical varieties (Fig. 13b). The examination shows that the vibrations of radar towers could be mitigated by filtering high wave numbers if the data coverage in the azimuth direction is at a constant range and sufficient for spectral analysis, such as FFT, which is generally satisfactory for tropical cyclones, such as Typhoon Goni, during the antenna oscillation period.

## 5. CONCLUSIONS

In this study, the phenomena of antenna oscillations and reflectivity oscillations caused by extremely strong wind speeds are investigated using data from the ISHI C-band Doppler radar operated by the JMA. The radar recorded elevations oscillated with a maximum amplitude of  $0.4^\circ$  at a  $-0.1^\circ$  elevation. The oscillation phenomenon was reflected in the reflectivity and Doppler velocity fields as Typhoon Goni's eyewall encompassed Ishigaki Island. The predominant oscillation period is approximately 0.25-0.33 s according to a FFT analysis. Additionally, there are two antenna oscillation periods. Between these two oscillation periods, the oscillation phenomenon disappears with decreasing wind speeds when Typhoon Goni's eye moved over the radar site. Regarding the reflectivity field oscillation, the antenna oscillation exhibits a feature that is out of phase and generally consistent with the vertical varieties of reflectivity. The Doppler velocity field is also influenced by the antenna oscillations that show alternating positive and near zero value features in the moat and spiral rainband regions. Compared to the reflectivity field, the oscillation phenomenon is relatively unobvious due to small vertical varieties in the Doppler velocity field.

With maximum amplitudes of elevations from wave numbers 45-60 that are greater than approximately  $0.02^\circ$  occurring between 1010 UTC and 1210 UTC and between 1340 UTC and 1430 UTC during Typhoon Goni's passage, the corresponding wind speeds are greater than  $50 \text{ m s}^{-1}$ , indicating a minimum wind speed for the occurrence criterion of the antenna oscillation. Consequently, it is suggested that the wind speed criterion for the

occurrences of antenna oscillations is approximately  $50 \text{ m s}^{-1}$  for the ISHI radars. However, the criteria of wind-induced antenna oscillations result from the vibrational effect of buildings that are closely related to the structure, material, height, and weight of the radar tower. The vibrational effect could be adequately mitigated if extremely strong wind conditions are considered for the design of radar towers.

To mitigate the influences of antenna oscillations on the radar observations, the QC procedure is proposed using a high-pass filter. The vibrations of the radar towers could be mitigated by filtering high wave numbers from wave numbers 45-60. The data coverage in the azimuth direction in a constant range is sufficient for spectral analysis, such as FFT, which is generally satisfactory for tropical cyclones such as Typhoon Goni during the antenna oscillation period. The estimated fundamental vibration periods are comparable to the predominant period analyzed from the reflectivity observations with values of 0.33 s and 0.5 s, respectively. Therefore, the results essentially agree with the expectation of wind-induced vibrations on a building. The vibrational effect of buildings that are closely related to the structure, material, height, and weight of the radar towers could be adequately mitigated if extremely strong wind conditions are considered in the design of radar towers. In the future, detailed oscillation simulations and analyses can be further conducted with wind tunnel tests to provide solutions for mitigating the vibrational effects of radar towers under extremely strong wind conditions.

## 6. ACKNOWLEDGMENTS

The authors thank the Japan Meteorological Agency for providing the radar data and Central Weather Bureau for providing the computing resources. This research is supported by the Ministry of Science and Technology of Taiwan, Republic of China under grants 107-2625-M-052 -001 and 108-2625-M-052-002.

## 7. REFERENCES

Browning, K. A., and R. Wexler, 1968: The determination of kinematic properties of a wind field using Doppler radar. *J. Appl. Meteor.*, **7**, 105–113.

Chang, P. -L., P. -F. Lin, B. J. -D. Jou, and J. Zhang, 2009: An application of reflectivity climatology in constructing radar hybrid scans over complex terrains. *J. Atmos. Oceanic Technol.*, **26**, 1315–1327.

—, W. -T. Fang, P. -F. Lin, and M. -J. Yang, 2019: A Vortex-based Doppler velocity dealiasing algorithm for tropical cyclones. *J. Atmos. Oceanic Technol.*, **0**, <https://doi.org/10.1175/JTECH-D-18-0139.1>

Dazhang, T., S. G. Geotis, R. E. Passarelli Jr., A. L. Hansen, and C. L. Frush, 1984: Evaluation of an alternating-PRF method for extending the range of unambiguous Doppler velocity. *Preprints, 22d Conf.*

*on Radar Meteorology*, Zurich, Switzerland, Amer. Meteor. Soc., 523–527.

Frush, C. L., 1991: A graphical representation of the radar velocity dealiasing problem. *Preprints, 25th Int. Conf. on Radar Meteorology*, Paris, France, Amer. Meteor. Soc., 885-888.

Garcia-Rivera, M. Jose, 2018: Hurricane Maria in Puerto Rico: Structure and intensity evolution prior to landfall. *33rd Conference on Hurricanes and Tropical Meteorology*, American Meteorological Society (AMS), Ponte Vedra, FL, US.

Kossin, J. P., and W. H. Schubert, 2001: Mesovortices, polygonal flow patterns, and rapid pressure falls in hurricane-like vortices. *J. Atmos. Sci.*, **58**, 2196–2209.

Lagos, R., and M. Kupeer, 2012: Performance of high-rise buildings under the February 27th 2010 Chilean earthquake. *Proceedings of the International Symposium on Engineering Lessons Learned from the 2011 Great East Japan Earthquake*. Tokyo, Japan, pp. 1754–1765.

Lee, W. -C., B. J. -D. Jou, P. -L. Chang, and F. D. Marks Jr., 2000: Tropical cyclone kinematic structure retrieved from single-Doppler radar observations. Part III: Evolution and structure of Typhoon Alex (1987). *Mon. Wea. Rev.*, **128**, 3982–4001.

—, —, —, and S.-M. Deng, 1999: Tropical cyclone kinematic structure retrieved from single-Doppler radar observations. Part I: Interpretation of Doppler velocity patterns and the GBVTD technique. *Mon. Wea. Rev.*, **127**, 2419–2439.

Lhermitte, R. M., and D. Atlas, 1962: Precipitation motion by pulse Doppler. *Proc. Ninth Weather Radar Conf.*, Kansas City, Amer. Meteor. Soc., 218-223.

Lhermitte, R. M., and D. Atlas, 1962: Precipitation motion by pulse Doppler radar. *Proc. Ninth Weather Radar Conf.*, Kansas City, Amer. Meteor. Soc., 218-223.

Lehenbauer, J. S. Tongue, and E. E. Clothiaux, 1998: Detection of nonprecipitating clouds with the WSR-88D: A theoretical and experimental survey of capabilities and limitations. *Wea. Forecasting*, **13**, 1046–1062.

Ryzhkov, A. V., P. Zhang, R. Doviak, and C. Kessinger, 2002: Discrimination between weather and sea clutter using Doppler and dual-polarization weather radars. *Proc. 27th General Assembly of the International Union of Radio Science*, Maastricht, Netherlands, International Union of Radio Science, F1.P.3.

Shimada, U., M. Sawada, and H. Yamada, 2018: Doppler radar analysis of the rapid intensification of Typhoon Goni (2015) after eyewall replacement. *J. Atmos. Sci.*, **75**, 143–162.

Velden, C., T. Olander, D. Herndon, and J. P. Kossin, 2017: Reprocessing the most intense historical tropical cyclones in the satellite era using the advanced Dvorak technique. *Mon. Wea. Rev.*, **145**, 971–983.

Warde, D.A., and S.M. Torres, 2017: Staggered-PRT sequences for Doppler weather radars. Part II: Ground clutter mitigation on the NEXRAD network using the CLEAN-AP filter. *J. Atmos. Oceanic Technol.*, **34**, 703–716.

Wu, C. -C., T. -H. Yen, Y. -H. Kuo, and W. Wang, 2002: Rainfall simulation associated with Typhoon

Herb (1996) near Taiwan. Part I: The topographic effect. *Wea. Forecasting*, **17**, 1001–1015.

—, and Y. -H. Kuo, 1999: Typhoons affecting Taiwan: Current understanding and future challenges. *Bull. Amer. Meteor. Soc.*, **80**, 67–80.

Xu, P., C. Xiao, and J. Li, 2014: Research on relationship between natural vibration periods and structural heights for high-rise buildings and its reference range in China. *International Journal of High-Rise Buildings*, **3**(1), 49–64. <https://doi.org/10.21022/IJHRB.2014.3.1.049>.

Yang, B., Y. Wang, and B. Wang, 2007: The effect of internally generated inner-core asymmetries on tropical cyclone potential intensity. *J. Atmos. Sci.*, **64**, 1165–1188.

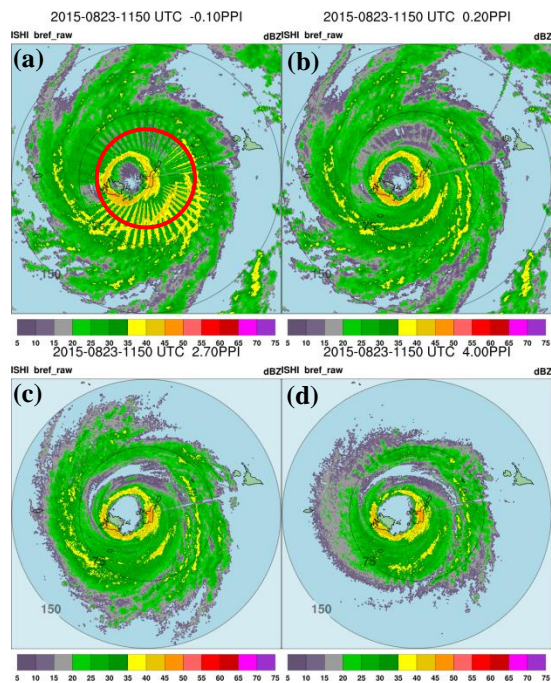


Figure 1. An example of reflectivity from the ISHI radar at 1150 UTC on 23 Aug 2015. (a)  $-0.1^\circ$ , (b)  $0.2^\circ$ , (c)  $2.7^\circ$ , and (d)  $4.0^\circ$ . The radar position is indicated by a red dot and the reflectivity data in the range of 50 km from the radar site in (a) will be used for the reflectivity oscillation analyses in Fig. 4.

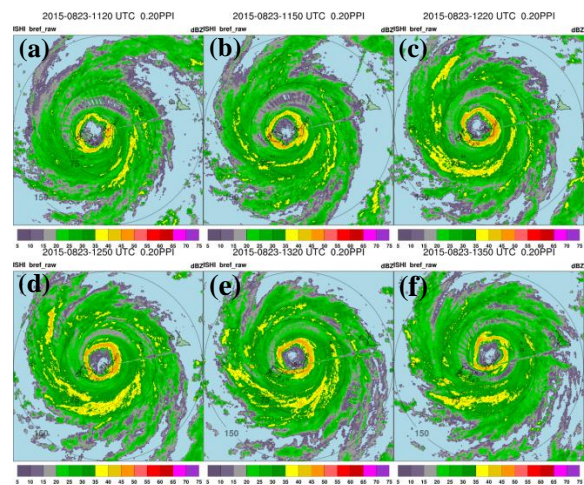


Figure 2. The temporal evolutions of the reflectivity field from the ISHI radar at the  $0.2^\circ$  elevation from (a) 1120 (b) 1150 (c) 1220 (d) 1250 (e) 1320 (f) 1350 UTC on 23 Aug 2015. The radar position is indicated by a red cross.

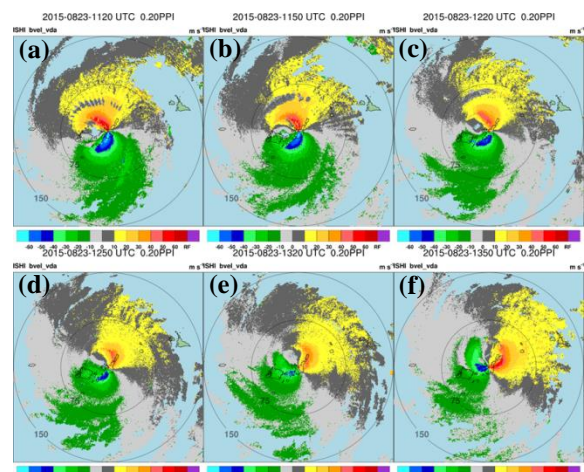


Figure 3. Same as Fig. 2 except for Doppler velocity field.

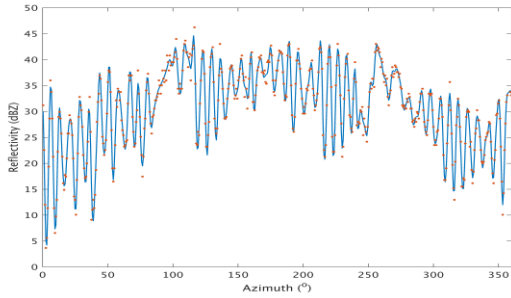


Figure 4. Azimuthal distributions of reflectivity in the range of 50 km from the radar site (as shown in Fig. 1a) at 1150 UTC on 23 Aug. 2015. The red dots indicate the observed reflectivities, and the associated blue curve is composed from the wave numbers calculated with the FFT analysis.

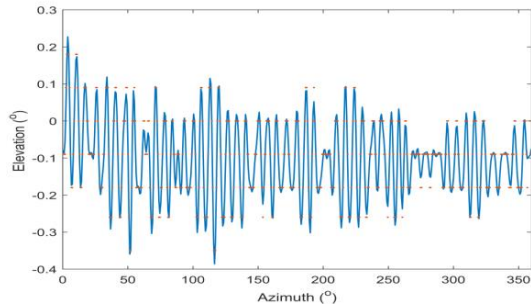


Figure 5. Same as in Fig. 4 except for the azimuthal distribution of elevations at  $-0.1^\circ$  elevation. The red dots indicate the recorded elevations, and the associated blue curve is composed from the wave numbers calculated with the FFT analysis.

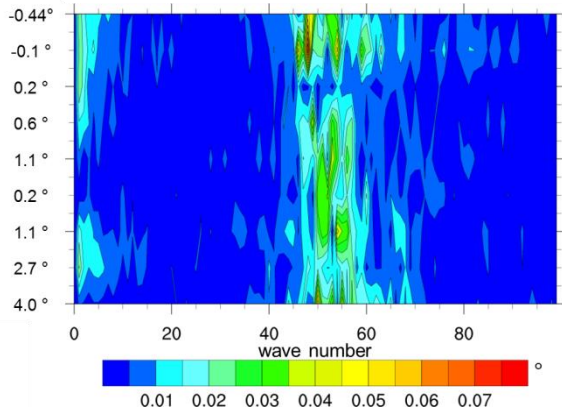


Figure 6. Elevation amplitudes with different wave numbers and preset elevations from  $-0.44^\circ$  to  $4.0^\circ$  at 1150 UTC on 23 Aug 2015.

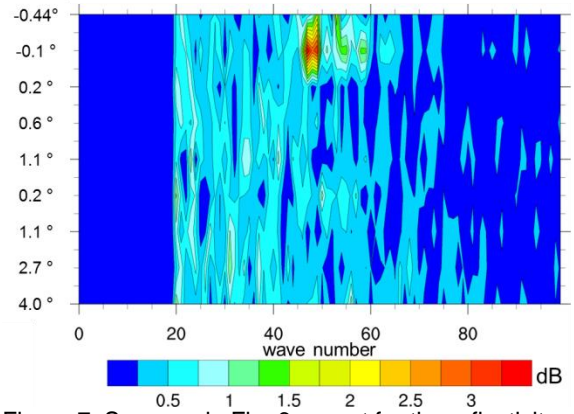


Figure 7. Same as in Fig. 6 except for the reflectivity amplitudes.

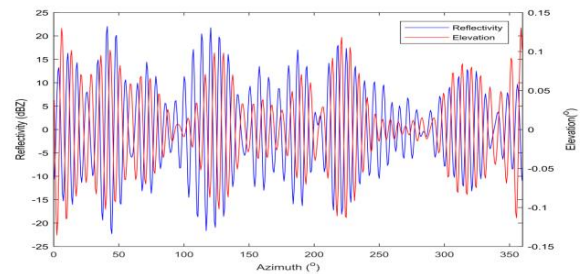


Figure 8. Azimuthal distributions of reflectivity and elevation amplitudes composed from wave numbers from 45 to 60.

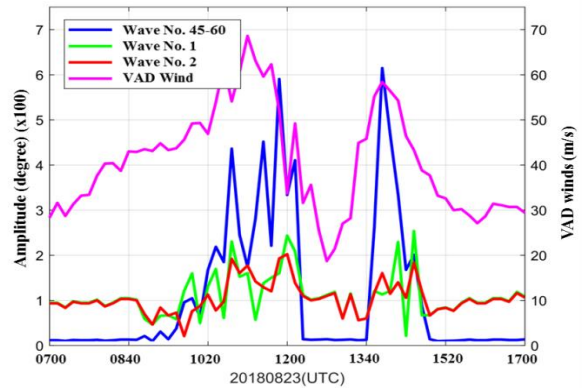


Figure 9. Temporal distributions of antenna amplitudes from the maximum amplitude of wave numbers 45-60 (blue), amplitude of wave number 1 (dark green), amplitude of wave number 2 (red), and VAD winds (fuchsia), which are indicated by different curves.

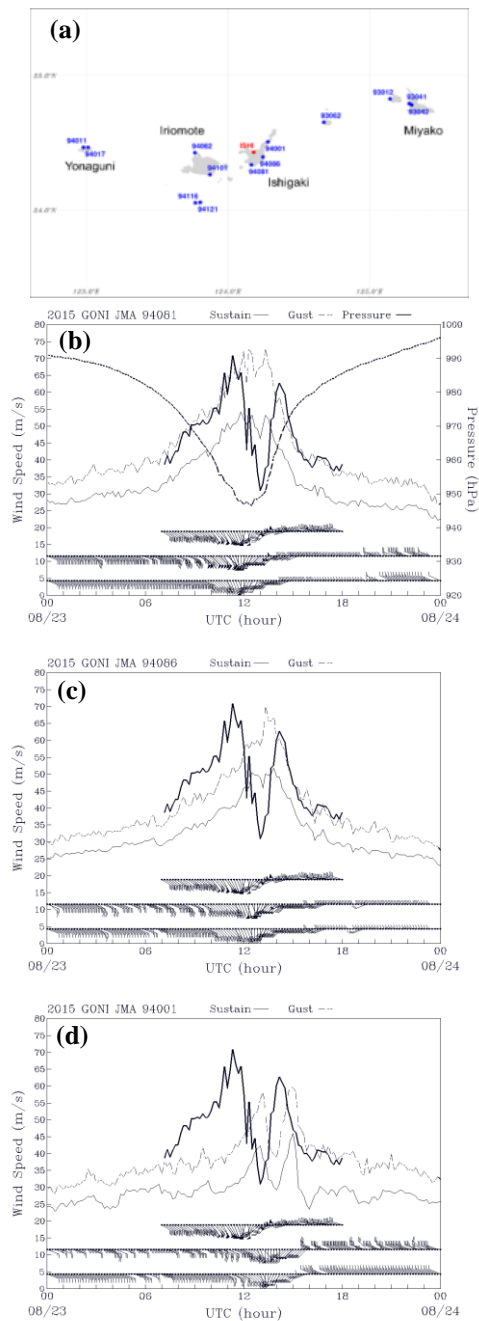


Figure 10. (a) Locations of weather stations on Ishigaki, Miyako, Iriomote, and Yonaguni Islands and temporal distributions of 10-min sustained and gust winds and pressure observed at stations (b) 94081, (c) 94086, and (d) 94001 on Ishigaki Island.

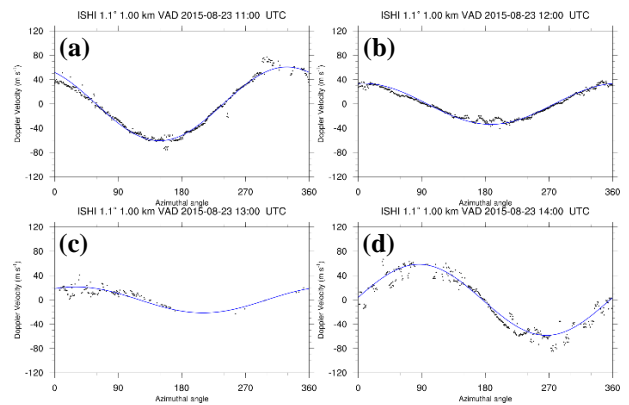


Figure 11. Examples of VAD analyses from 1100 UTC to 1400 UTC on 23 Aug 2015. The blue lines indicate the cure fit for VAD analyses.

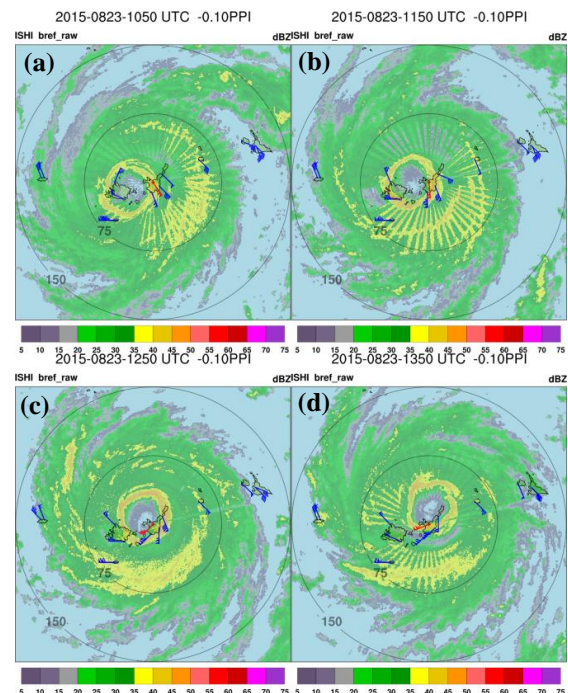


Figure 12. Spatial wind distributions from surface winds (blue color) and VAD winds (red color) from 1150 UTC to 1350 UTC on 23 Aug 2015.

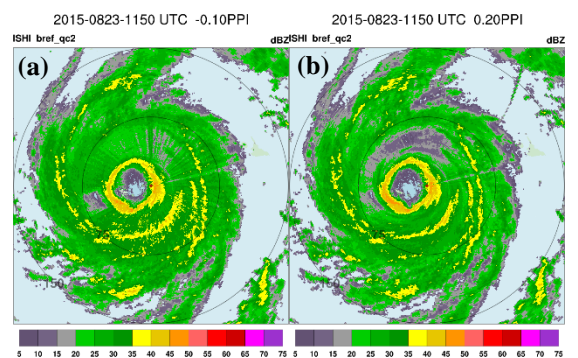


Figure 13. Example of reflectivity at 1150 UTC 23 on Aug 2015 after the high-pass filter QC procedure at (a)  $-0.1^\circ$  and (b)  $0.2^\circ$  elevations.